

ARTICLE OPEN



Initial atomic-scale oxidation pathways on a Ni–15Cr(100) alloy surface

William H. Blades^{1,2}, Matthew R. Barone^{1,3} and Petra Reinke¹✉

To understand the atomistic phenomenon behind initial oxidation processes, we have studied the nanoscale evolution of oxide growth prior to the formation of a complete layer on a Ni–15 wt%Cr(100) alloy surface using scanning tunneling microscopy/spectroscopy (STM/STS). At the onset of oxidation, a NiO superlattice forms oxide wedges across the step edges, eventually growing across the terraces. The completion of the NiO layer is followed by nucleation of the next layer, which always commences at the groove site of the superlattice. The Cr-oxide formation initiates as disk-shaped oxide particles early in the oxidation process, which Monte Carlo simulations reveal are likely caused by Cr clustering across the alloy surface. Upon further oxidation, a Cr(100)-p(2 × 2)O reconstructed surface is observed, indicating phase separation of Cr predicated the formation of the passive Cr-oxide film. The STS results vary across the oxide–alloy interface and between each oxide, providing greater insight into the origins of electronic heterogeneity and their effect on oxide growth. Using these data, we propose an oxidation model that highlights the growth of partial oxide layers on Ni–Cr(100) alloys within the pre-Cabrera–Mott regime.

npj Materials Degradation (2021)5:17; <https://doi.org/10.1038/s41529-021-00164-7>

INTRODUCTION

Early-stage oxidation of metals commences with the nucleation and growth of partial oxide layers or islands on the surface and results in significant structural and chemical changes at the metal–oxide interface^{1–6}. These changes to the metal–oxide interface predicate the development of a complete and ideally corrosion-resistant oxide layer. Specifically, Ni–Cr alloys have gained considerable attention in recent years due to their excellent mechanical properties and the superior corrosion resistance afforded by the growth of a passive chromia layer^{7–15}. Despite the interest in this alloy system, significant gaps still exist in our understanding of the transition between the initial adsorption of oxygen and the subsequent growth of a complete oxide layer. Models have been developed, such as the Cabrera–Mott model, that specifically considers the growth kinetics of oxide layers between 1 and 10 nm in thickness^{1,16,17}. While Cabrera–Mott has been used to successfully describe the temperature-dependent thickening of oxide films and their growth via electric-field driven ion transport, discrepancies arise due to the assorted oxidation pathways exhibited by transition metal alloys, e.g., Ni–Cr. Therefore, by examining the growth of partial oxides during the pre-Cabrera–Mott regime defined here as the regime prior to the formation of a complete oxide layer, the fundamental phenomena that drive early-stage oxidation can be understood.

Given the chemically distinct nature of Ni and Cr, oxide growth on Ni–Cr alloys is governed by the competing oxidation pathways of the two reactive elements. At elevated temperatures, oxidation of Ni(100) begins with the dissociative chemisorption of O₂ and the formation of p(2 × 2)O and c(2 × 2)O ordered adlayers^{18–22}. The chemisorbed phases trigger step-edge faceting, which kinetically hinders oxide nucleation at the step edges and NiO is only observed after large O₂ doses^{18,19}. For Cr(100), a variety of different ordered oxygen adlayers and surface reconstructions have been reported after oxygen exposure^{23–28}. It has been

postulated that variations in sample surface preparation are responsible for the disparities²³. While the initial onset and progression of monolayer oxygen coverage is unresolved, the formation of chrome-oxide has been shown to initiate by the incorporation of oxygen atoms into the relatively open BCC Cr(100) surface. After a complete layer is formed the initial oxide growth is dominated by oxygen anion transport at $T_{ox} < 300$ °C and by metal cations at elevated temperatures²⁸. The unique reaction pathways of the Ni(100) and Cr(100) surfaces suggest that alloying will result in distinctive oxidation processes different from those of the pure constituent metals.

The complex interplay between thermodynamic and kinetic factors in the oxidation of the Ni–Cr system leads to competition between oxide species. This is also expressed in a variation of the metal–oxygen bond energies moving from pure metals to alloys, and oxides with different structures and chemistry as recently calculated by Chien et al.²⁹. Which oxide will form, and their relative concentration with respect to the total oxide population, depends on temperature, alloy composition, oxygen partial pressure, and crystallographic orientation. Notably, not all of these factors have been studied in detail, and the present work targets the initial oxidation steps where the competition between oxide species is readily apparent. The lower nucleation barrier for NiO due to cube-on-cube epitaxy is generally assumed to kinetically favor the nucleation of NiO compared to chromia albeit direct experimental observation of the initial oxidation steps as a function of crystallographic orientation is missing¹¹. The oxidation of a Ni–5 wt%Cr(100) alloy at 300 °C revealed oxide island growth after small sequential O₂ exposures, highlighting the addition of Cr removes the temperature induction period for oxide growth on Ni(100) surfaces^{10,18}. A surface diffusion model, where oxygen atoms diffused to the oxide growth front, was developed and found a short screening length of 0.3–0.4 nm, suggesting oxide island growth at these temperatures is localized to the island edge¹⁰. At higher temperatures, oxidation is driven

¹Department of Materials Science and Engineering, University of Virginia, Charlottesville, VA, USA. ²Ira A. Fulton Schools of Engineering, Arizona State University, Tempe, AZ, USA.

³Department of Materials Science and Engineering, Cornell University, Ithaca, NY, USA. ✉email: pr6e@virginia.edu

by the transport of metal atoms, as shown during the initial oxidation of a Ni–10 at%Cr(100) sample at 450 °C⁹. An operando high-resolution transmission electron microscopy study confirmed that NiO growth is kinetically favored, as compared to the more thermodynamically preferred Cr₂O₃, due to the rapid surface diffusion of Ni atoms across NiO within this compositional space^{8,9}. Partially closed subsurface layers of Cr₂O₃ were observed beneath the NiO layers at $T_{\text{ox}} = 700$ °C, and when [Cr] = 20 at% these initially disjointed ‘subsurface islands’ form a complete Cr₂O₃ layer⁸. The manner in which the NiO and Cr₂O₃ evolve as a function of both temperature and composition reflect the diverse nature of oxide growth on Ni–Cr(100) surfaces and indicate that more work is required if the competition between the different oxidation pathways is to be fully understood.

Recently, our work has focused on the nanoscale observation of Ni(100) and Ni–Cr(100) surface oxidation by studying the sequential oxidation of alloy thin films (8–12 wt%Cr) grown in ultra-high vacuum (UHV) with STM (scanning tunneling microscopy) and STS (scanning tunneling spectroscopy)^{7,30}. The initial oxidation on Ni–Cr(100) begins with the nucleation and growth of NiO along the step edges and a dense population of small oxide particles on the terraces. The NiO formed low-angle grain boundaries with respect to the Ni–Cr(100) surface and a distinct NiO–NiCr(7 × 8) superlattice was observed across the step edges, while a NiO–NiCr(6 × 7) superlattice was found on the terraces^{7,31}. Concurrently, a variety of chemisorbed phases and large oxide nodules, assigned as Cr₂O₃ or NiCr₂O₄, grew on the terraces. The geometric structure of the chemisorbed phases, which is reminiscent of a Cr(100)-O reconstruction, strongly suggested the segregation of Cr at the surface, however, no atomic spacing could be measured for confirmation. STS measurements combined with a statistical analysis of the surface’s electronic structure revealed significant spatial variability in the surface band gap and confirmed the compositional and structural heterogeneity of the oxide–alloy interface and surface. The usual assumption of a homogenous electric field between the alloy and oxide surface is therefore insufficient to describe oxide growth once a complete oxide layer is formed.

Complementary STM work has been done by Ma et al. on an oxidized Fe–18Cr–13Ni(100) austenitic stain steel surface, with the goal to understand the relation between heterogeneity in the

initial oxidation steps and pitting events at a later stage⁶. The emergence of ordered vacancy structures in the metal surface is unique and occurs in parallel with the onset of oxidation at step edges where Cr-oxide and Fe-oxide emerge at a longer exposure. Complex step edge faceting is observed with convex and concave regions developing and is unique to this ternary system. On the other hand—even though austenitic stainless steel is a ternary system its propensity to form a large variety of surface structures is surprisingly more limited than for Ni–Cr(100).

Experiments that target the initial progression of oxide growth, combined with surface-sensitive techniques, are necessary if the complex nature of early-stage oxidation is to be understood. To this end, STM and STS have been employed to capture the atomic-scale mechanisms of surface oxidation on a Ni–15 wt%Cr(100) sample at 500 °C and will be discussed in detail. The Cr oxidation pathway starts by nucleating flat disk-like particles, their size driven by the local distribution of Cr-clusters in the first two (100) planes of the surface. As oxidation progresses phase separation of BCC Cr(100) is observed. Adjacent to these segregated regions is oxide rows and faceted oxide features, which are attributed to the passive Cr-oxide pathway. Initially nucleating at the step edges, the NiO rapidly saturates the surface and thickens, with the next layer initiating growth at the NiO superlattice groove site. Spatially resolved DOS (density of states) maps reveal the origin of this behavior is attributed to the heterogeneity across the NiO superlattice, imprinted by the alloy–oxide interface. These data are used to build a model for the nanoscale growth of the partial oxide layers Ni–Cr(100) surfaces. Together, these details on the evolution of the surface’s electronic and geometric structure have further illuminated the nuances of early-stage oxidation on Ni–Cr alloys within the pre-Cabrera–Mott regime.

RESULTS

General trends in oxidation

STM images of the Ni–15 wt%Cr(100) surface prior to oxidation and after each exposure step are displayed in Fig. 1. The onset of oxidation, 7 L of O₂ exposure at 500 °C, results in significant changes to the surface of the alloy. Oxide growth initiates with step-edge faceting driven by a partial step-edge decoration of a

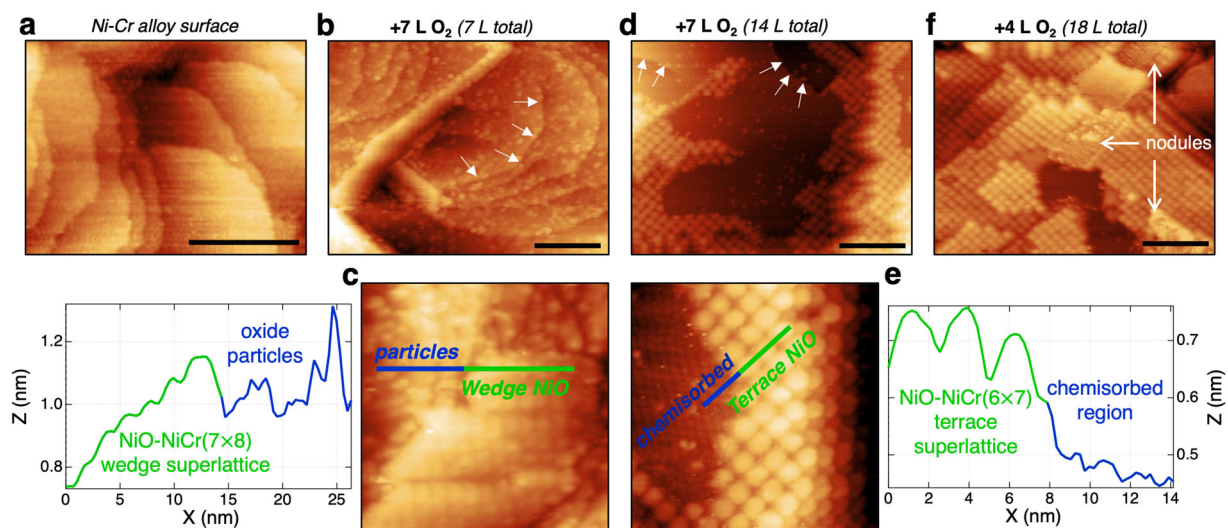


Fig. 1 An overview of the oxidation steps and features on the surface. Topography of the alloy surface prior to oxidation is given in (a). The progression of oxidation after cumulative O₂ exposures at 500 °C of 7 L (b), (c), 14 L (d), (e), and 18 L (f). All scale bars are 20 nm. The white arrows indicate step edges that have not faceted and are still curved despite oxygen exposure. Image (f) was measured at $V_{\text{bias}} = 0.25 V_f$, $I_t = 0.5$ nA, (b), (c), (d) and (e) at $V_{\text{bias}} = 2.0$ V, $I_t = 0.1$ nA, and (f) at $V_{\text{bias}} = 3.0$ V, $I_t = 0.1$ nA. The images in panels (c) and (e) are both 30×30 nm² and show the different features after cumulative 7 L and 14 L exposures, respectively. Line scans of each feature at these oxidation steps are provided.

NiO–NiCr(7 × 8) superlattice—NiO wedge—while oxide particles, tentatively assigned as Cr-oxide particles, have nucleated and grown across the terraces and some step edges as seen in Fig. 1b, c^{7,18,19}. The assignment of the step edge and terrace oxide with square structure as NiO is based on (i) comparison with the structure of NiO on Ni(100) in our laboratory and reported in the literature^{19,31}, (ii) reported enhanced nucleation of cubic NiO on (100) surfaces for alloys in a similar concentration range and temperature range⁹, (iii) a band gap which is commensurate with NiO and excludes co-nucleation of CrN (metallic).

After 14 L cumulative exposure, the NiO wedges have thickened and NiO has grown across the terraces, taking a different epitaxial relationship with the alloy by forming a NiO–NiCr(6 × 7) superlattice, Fig. 1d, e. The NiO superlattices and their effect on the alloy surface have been discussed extensively in the following reference for alloys with smaller Cr-concentrations⁷. At this exposure of 14 L, the Cr-oxide particles are no longer present on the surface and are substituted by a variety of chemisorbed oxygen adlayers seen between the boundaries of the NiO layers, Fig. 1e. Additional oxidation, +4 L (18 L cumulative), causes greater NiO surface coverage, the emergence of more second layer NiO, a reduction in the surface area covered by ordered chemisorbed adlayers, and the growth of sizable oxide nodules⁷, which are also marked in Fig. 1f. It is evident from these images that the Ni–Cr(100) oxidation pathway is complex, and will therefore be discussed in a step-by-step manner in this report starting with a closer look at the oxide clusters observed in the very first oxidation step.

Cr-oxide particles

The NiO oxidation pathway presents clearly in the topography images post-exposure, and the oxidation of Cr appears to begin with the nucleation and growth of oxide particles. To better understand the particle geometry, height and area distributions are measured over flat segments of the alloy surface, represented by the 3D topography image in Fig. 2a. The height distribution in Fig. 2b reveals an apparent height of approximately 1.25 Å, while the area distribution obtained via the MATLAB segmentation code is shown in Fig. 2c. Given the shallow apparent height, another method for the quantification of particle dimensions was employed, and the particles were assumed to be flat disks, where the $Area = \pi r^2$ and radius r were determined by numerous line scans. This second method yielded an area distribution in excellent agreement with the distribution obtained by the segmentation code, therefore modeling the Cr-oxide particles as flat disks and islands are acceptable.

The Cr-oxide particles have been observed in our prior work on Ni–Cr(100) oxidation and are thermally stable with respect to annealing at 600 °C, contrasting NiO which was reduced and thus removed from the surface during this heat treatment⁷. Similar particles have also been previously reported during thermal oxidation of pure Cr thin films³². Our STM results show the Cr-oxide particles preferentially populate across the alloy terraces and some step edges, marked by white arrows in Fig. 1b. No such particles are found on pure Ni surfaces supporting the interpretation as Cr-oxide or at least mixed Cr–Ni oxides. The extent of NiO step-edge coverage is higher on Ni–Cr(100) samples with lower Cr concentration⁷, suggesting that step-edges with a higher local Cr concentration nucleate Cr-oxide particles instead of undergoing NiO-driven step faceting. Essentially, NiO formation at the step edges competes with the nucleation of Cr-oxide particles, which also prevents step edge faceting as seen in Fig. 1. However, STM and STS do not deliver directly compositional information in the absence of a well-recognized surface structure (e.g., NiO), so we assign these features as Cr-rich oxide particles, as opposed to asserting they are purely Cr-based. Certainly, the initiation of Cr-oxidation is dominant on the terraces and step edges with higher Cr concentration, therefore we propose here that the presence of

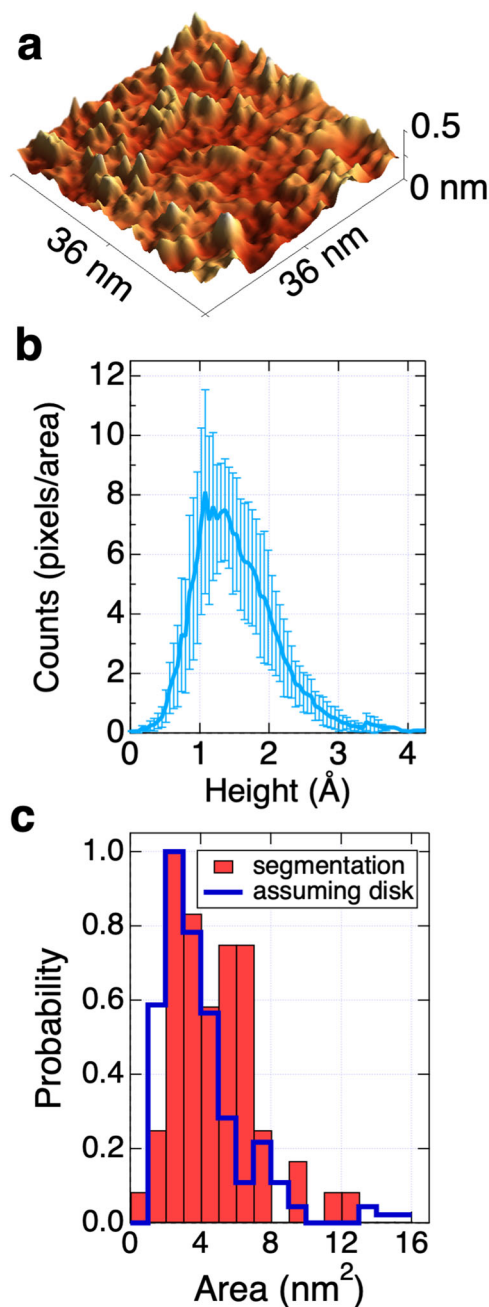


Fig. 2 Geometric structure of the oxide particles. **a** 3D topography image showing the oxide particles present after 7 L of oxygen exposure along with **(b)** their height distribution. The area distribution of these particles is summarized **(c)** and was determined two different ways, (i) via gray-scale segmentation (see supplementary information) and (ii) line scans combined with the assumption that the particles are disks ($A = \pi r^2$), which was used to translate radius into area distributions. The topography image was taken at $V_{\text{bias}} = 2.0$ V, $I_t = 0.1$ nA. The error bars in **(b)** were calculated using standard error.

Cr-oxide particles can be linked to the distribution of Cr-atoms in the Ni–Cr(100) solid-solution surface.

To develop a qualitative understanding of oxide particle formation on the surface after the 7 L exposure, we developed a MATLAB code that visualizes the stochastic distribution of Ni and Cr atoms within the first two layers of a substitutional solid-solution FCC(100) surface for a predefined alloy stoichiometry. The second layer is included to build a more realistic surface model

which is suitable for future computational work to describe the surface chemistry. The distribution of Cr atoms on the surface can be described with various statistical tools including pair correlation functions, however, for the purpose of the current manuscript, we chose to specifically illustrate the interconnectedness of Cr-atoms at the surface by assessing the cluster dimensions. The prevalence of dimer, trimer, tetramer, and pentamer-sized Cr-clusters in the two surface layers is displayed in Fig. 3a for a variety of alloy compositions. Several simulations were run for each alloy composition, and the number of Cr-clusters (n) of a given atom size is shown as a function of at%Cr. The details of cluster counting are given in Supplementary Fig. 1. The number of Cr-clusters reaches a maximum when the composition (cluster-size) is 16 at%Cr (dimer), 19 at%Cr (trimers), 20 at%Cr (tetramer), and 22 at %Cr (pentamer). The contributions from clusters with $n > 5$ increase rapidly for Cr concentrations exceeding 15 at%. A closer look at the cluster distributions for a Ni-15 wt%Cr(100) alloy is provided in Fig. 3b, c.

The average cluster size increases with the addition of a second layer, which is summarized in the histogram presented in Fig. 3b. This result is expected given that the addition of a second layer increases the coordination number and inherently leads to larger and more realistic clusters. The second layer can be interpreted as a Cr-atom reservoir that feeds the growth of nanoscale surface oxides at these temperatures. A spatial representation of the first and second plane clusters on a Ni-15 wt%Cr(100) is included in Fig. 3c. The filamentous Cr-surface clusters are preferred oxygen adsorption sites since DFT has shown that Cr is a preferential bonding site for oxygen in Ni-Cr alloys^{12,33}. The larger propensity of extended filamentous Cr-clusters for higher Cr-content in the alloy rapidly increases the likelihood of O-adsorption at or very near a Cr site on the surface. Consequently, the Cr-surface clusters

can be seen as precursors for oxide islands and particles formed in the initial reaction steps. Indeed, the distribution of the Cr within the first few layers of the alloy is likely responsible for the initiation of the passive chromia layer, while the NiO nucleation is driven by the cube-on-cube epitaxy. A more detailed study of the re-organization of Cr within the surface layer in response to oxygen adsorption and the development of chemical potential-driven diffusion is in progress.

Fourteen Langmuir of cumulative oxidation

Once the sample is exposed to a cumulative 14 L of O₂, the oxide particles are no longer present. Instead, ordered chemisorbed oxygen adlayers have emerged across the surface and a complex mixture of different structures and domains is present. A few segments of curved alloy step edges are retained and covered with these adlayers, marked by white arrows in Fig. 1d. Unlike the $c(2 \times 2)$ reconstruction on pure Ni(100) the chemisorbed adlayers observed here do not induce step edge faceting. Images of the surface reconstructions/adlayers (generally referred to as “chemisorbed regions”) are provided in Supplementary Fig. 2. None of these surface structures exactly correspond to known chemisorption adlayers or surface oxides for Ni or Cr surfaces, however, some have general symmetries that are reminiscent of surface reconstructions observed on oxidized Cr(100) surfaces^{23–28}. However, the size of the unit cells and feature dimensions as measured from the STM images are significantly larger than atomic-scale models of simple surface reconstructions would require. The topographic surface features do not correspond to any known chemisorbed oxygen adlayer, alloy, or oxide-alloy interface, and STS yields an unusually broad distribution of band gap values centered at about 1.8 eV⁷. Indeed, these chemisorbed structures could be a collection of defects, vacancies, or

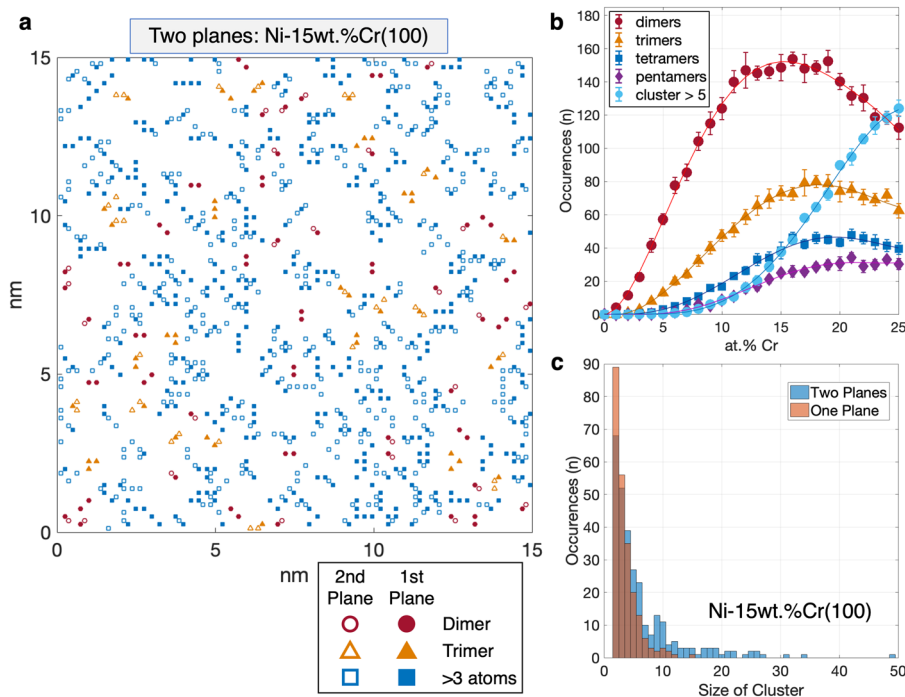


Fig. 3 Distributions of Cr atoms and clusters on the (100) surface of a random solid solution. **a** The visualization shows two Ni-15 wt%Cr planes of the alloy with dimers marked with red circles, trimers orange triangles, and tetramers or larger clusters with blue squares; a closed circle/triangle/square is chosen for atoms in the first plane, and an open circle/triangle/square marks atoms in the second plane. At least one atom for each cluster is positioned in the top layer (first plane), and single Cr atoms are omitted for clarity. The details of the calculation and cluster counting are described in the Supplementary Information. **b** Summarizes the occurrence of different cluster sizes as a function of Cr concentration in the top two (100) planes which are built of 100×100 atoms each. The histogram in **(c)** displays the size distribution of Cr clusters on the surface of the Ni-15 wt%Cr alloy if a single or two planes are taken into account. The error bars in **(b)** represent the standard deviation of the data point.

nanocavities, which have been reported for oxide–metal interfaces³⁴. A collection of these surface reconstructions is shown in Supplementary Fig. 2. These regions are most prominent after 14 L of exposure but disappear with the addition of just 4 L of O₂, which indicates that the chemisorbed oxygen adlayers are likely metastable, intermediate surface structures with unique oxygen coverages and distinctive interfacial relationships with the metal lattice below.

Eighteen Langmuir of cumulative oxidation

After an additional 4 L oxidation step (18 L cumulative), the aforementioned chemisorbed oxygen adlayer regions disappear, and a new set of surface structures emerge: a reconstruction/chemisorbed adlayer with a square unit cell, an oxide “row” structure, and a faceted oxide feature now dominate and mark the progression of the oxidation process. Figure 4a shows a high-resolution image of reconstruction/chemisorbed adlayer, an ordered surface structure that can be imaged with atomic resolution and is positioned in between the NiO edges. Line scans along the max-to-max positions reveal an average spacing of $6.0 \text{ \AA} \pm 0.1$ and a diagonal spacing of $8.2 \text{ \AA} \pm 0.1$ confirming the square geometry of the structure. Distributions of these data are provided in Fig. 4b. The spacings were compared with a variety of possible O-adsorbate surface structures on both, Ni(100) and Cr(100) surfaces, and the theoretical spacings and respective percent error (%) are provided in the table included in Fig. 4c³⁵. The Cr(100)-p(2 × 2)O ordered phase best fits the measured spacings, and a model surface structure is included as Fig. 4d where the p(2 × 2) unit cell is marked in gray. Note that this is a BCC (100) surface and not the FCC (100) surface of the Ni–Cr alloy. The green square illustrates the correspondence between the model and topography image, also marked with a green square in Fig. 4a. The deviation between the experiment and reported

theoretical values for Cr(100)-p(2 × 2)O is well within the experimental error. In this interpretation of the reconstruction, it is assumed that the oxygen atoms are imaged as depressions²⁷, which could be disputed, but does not change the comparison with dimensions of the p(2 × 2)O unit cell on a BCC (100) surface.

The presence of the atomically resolved adlayer highlights that a BCC Cr(100) lattice region is embedded within the FCC Ni–Cr (100) alloy surface and emphasizes oxidation induces phase separation of the alloy in the surface region. The Cr(100)-p(2 × 2)O surface section is rotated by ~27° with respect to the NiO lattice. It should be noted that we cannot see the oxide–alloy interface itself, therefore it is possible the BCC layer has a unique epitaxial relationship with respect to the surrounding FCC matrix^{36–39}. The presence of this Cr(100) phase is evidence that the surface composition of the alloy changes significantly after O₂ exposure and the alloy surface can no longer be considered simply as an FCC Ni–Cr(100) random solid solution. This analysis confirms the formation of areas with pure Cr surface layers, which form by phase separation from the alloy and present the characteristic Cr(100)-p(2 × 2)O surface.

At this 18 L of O₂ exposure step the Cr(100)-p(2 × 2)O surface dominates the regions between the NiO, and oxide rows and faceted-oxide features co-exist with the reconstruction and are shown in Fig. 5. These additional nanoscale oxide features offer significant challenges in their assignment and are discussed in this paragraph in more detail. Both features are commonly seen adjacent to the Cr(100)-p(2 × 2)O surface structure, and examples are included in Figs. 4a and 5a, b. Their proximity to known segregated regions of Cr(100), as well as their distinctive geometric and electronic structures compared to that of NiO, leads us to assign them to the Cr-oxidation pathway and tentatively ascribe them as “Cr-oxide rows” and “faceted Cr-oxide” layers, respectively. The “Cr-oxide rows” are geometrically distinct

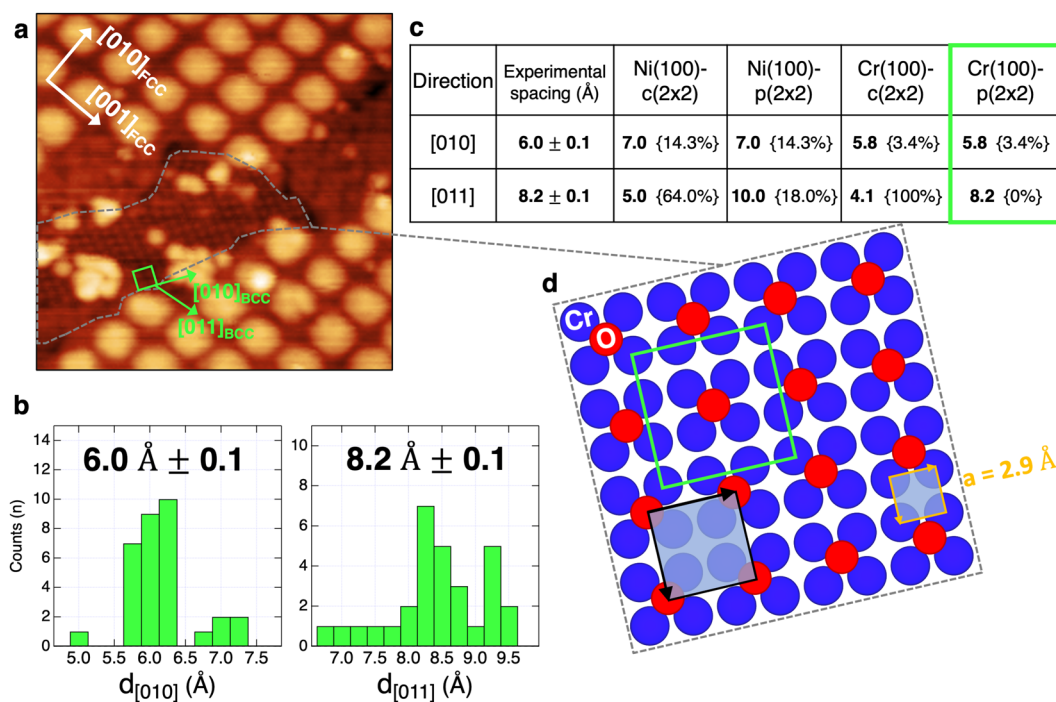


Fig. 4 Cr phase segregation. **a** Topography image after the 18 L oxidation step ($20 \times 20 \text{ nm}^2$). This oxidation step illustrates the segregation of Cr(100) and the FCC and BCC surface orientations are marked in the image, where the FCC directions are deduced from the NiO orientation relative to Ni as shown previously. The distributions in **(b)** give the maximum-maximum spacing along the [010]_{BCC} and [011]_{BCC} directions, respectively, with the average spacing given in each histogram. **c** Compares the surface geometry measured in the STM images to other surface structures known for Ni(100) and Cr(100) for various oxygen coverages. The table summarizes the surface dimensions and interatomic spacing with the {discrepancy} to the experimental data given for each structure model. **d** Model of the Cr(100) surface for the Cr(100)-p(2 × 2) phase, which has an excellent agreement with the experimental data. The STM topography image was taken at $V_{\text{bias}} = -3.0 \text{ V}$, $I_t = 0.1 \text{ nA}$.

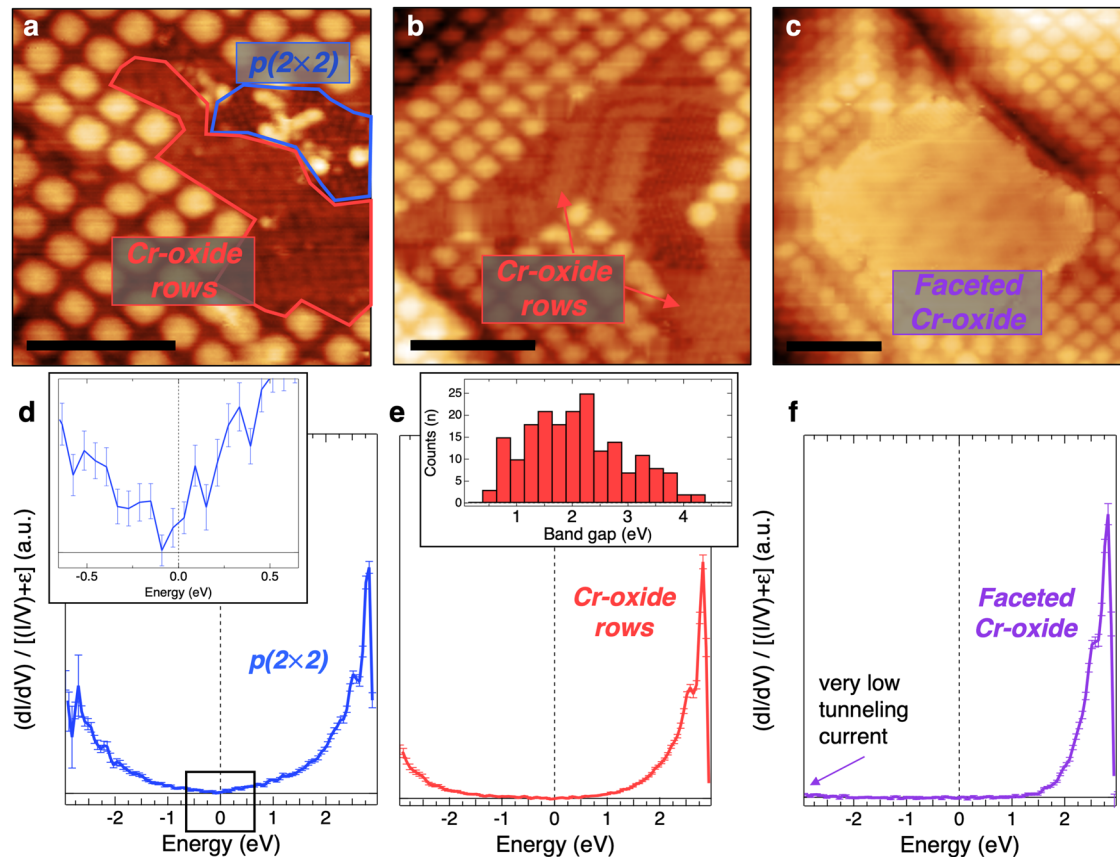


Fig. 5 Cr-oxide features and growth. Topography images of the Cr-oxide rows (a) and (b) and faceted Cr-oxide feature (c), tentatively assigned to the Cr-oxide pathway (detailed discussion of assignment in the text). The STS curves of each of these features are shown in (d)–(f). The STS for the $p(2 \times 2)$ and oxide rows in (d) and (e) were both recorded from their respective regions marked in the image (a). A close-up of the normalized spectra near the Fermi energy is included in (d) and a band gap distribution of the Cr-oxide rows is shown in (e). The STS for the faceted Cr-oxide, (f), was measured in the region marked in topography image (c). Image (a) was measured at $V_{\text{bias}} = -3.0$ V, $I_t = 0.1$ nA, while images (b) and (c) were measured at $V_{\text{bias}} = -3.0$ V, $I_t = 0.05$ nA. All scale bars are 10 nm. All error bars were calculated using standard error.

from the NiO and previously reported chemisorbed adlayers, and the spacings between the rows are quite varied as shown in Supplementary Figs. 3 and 4. The Cr(100)- $p(2 \times 2)$ O surface is nearly metallic, while the Cr-oxide rows have significant variability in their electronic structure with an average band gap of 1.9 ± 0.1 eV, as shown in Fig. 5d, e, respectively. The band gap is smaller than that for the bulk oxides but larger than the values observed for the chemisorbed adlayer regions. This leads us to interpret the oxide rows as a “transition state” between adsorbate and fully formed oxide with a bulk oxide signature. Figure 5c illustrates the “faceted Cr-oxide” features adjacent to the Cr(100)- $p(2 \times 2)$ O regions. The tunneling current from the filled states in STS is very small and indicative of the insulating nature of the oxide feature, Fig. 5f. A periodic surface structure with rectangular symmetry is observed when their filled states are measured with a rather high $V_{\text{bias}} = -3.5$ eV, which is included in Supplementary Fig. 4.

The chemical nature of these oxides remains open to interpretation and is challenging to resolve like most oxide surface structures. It has been demonstrated that $\text{Cr}_2\text{O}_3(100)$ surface configurations are susceptible to local oxygen content and oxygen partial pressure variations^{40–44}, and a simple feature matching approach might not be informative in this case. We propose that when taking into account both the electronic and geometric structure of the Cr-oxide rows and faceted Cr-oxide features and their proximity to regions of segregated Cr(100), that they are intermediate stages of Cr-oxide growth on the Ni–Cr(100)

surface. While we have assigned these two oxides to the overall Cr-oxidation pathway, we are hesitant to be more definitive about their stoichiometry and crystallography, hence the relatively vague nature of their labels as “Cr-oxides.” This result is in agreement with the generally reported observation that Cr_2O_3 growth on Ni–Cr alloys are slower than the formation of NiO during the initial stages of oxidation^{8,9,45}.

Ni oxidation pathway

The oxidation pathway leading to NiO nucleation and growth begins at the alloy step edges, presenting as a NiO–NiCr(7×8) superlattice, and as oxidation progresses the terraces become saturated with the NiO–NiCr(6×7) superlattice as a consequence of a cube-on-cube epitaxy⁷. As the total oxide coverage increases small areas of second and third layer NiO begin to appear. Figure 6a displays the topography image of the NiO after 18 L of oxygen exposure, and an image inset shows the emerging next layer. This layer is always seeded along with the NiO–NiCr(6×7) superlattice groove site. Small spherical protrusions can be seen between these grooves, as indicated by white arrows in the topography image, Fig. 6a, and could represent the nuclei of next layer growth. A line scan across these features is included in Supplementary Fig. 5. Indeed, the superlattice sites—grooves and top sites—differ subtly in the electronic structure of the valence band, which is seen in the grid STS DOS (density of states) map summarized in Fig. 6b. This figure was formatted from the spectroscopy results and is shown for $V_{\text{slice}} = -2.7$ eV. The variation in DOS across the

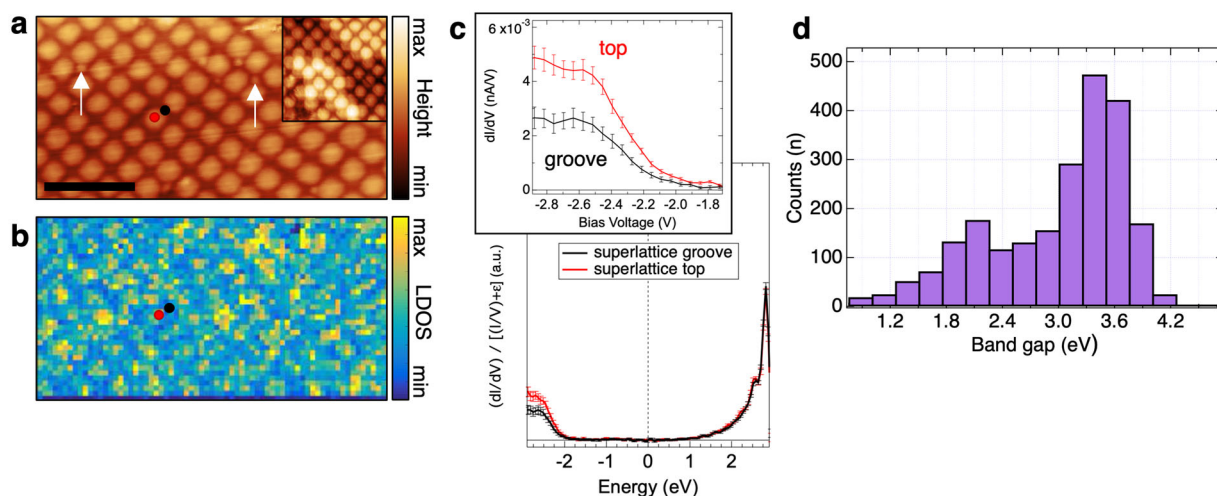


Fig. 6 Electronic heterogeneity of the NiO superlattice. Panel (a) is the topography image of the NiO–NiCr(100) superlattice structure and (b) the corresponding normalized dI/dV map (proportional to LDOS) at $V_{\text{slice}} = -2.7$ V. The image inset in (a) shows the orientation of the next NiO layer and is from a Ni–12 wt%Cr(100) sample shown here for comparison (image size 20×20 nm²). The white arrows point to small protrusions in the NiO positioned over the groove site of the superlattice. The red and black dots in the LDOS map represent the superlattice top site and the groove site, respectively, where the average, normalized dI/dV spectra shown in (c) were acquired. The inset above the normalized spectra shows the difference in the differential conductance of the respective sites. Panel (d) is a distribution of the band gap values extracted from the entire LDOS map shown in (b). Imaging conditions: (a) $V_{\text{bias}} = 2.0$ V, $I_t = 0.1$ nA, and the inset at $V_{\text{bias}} = -1.0$ V, $I_t = 0.1$ nA. The scale bar is 10 nm. The error bars in (c) were calculated using standard error.

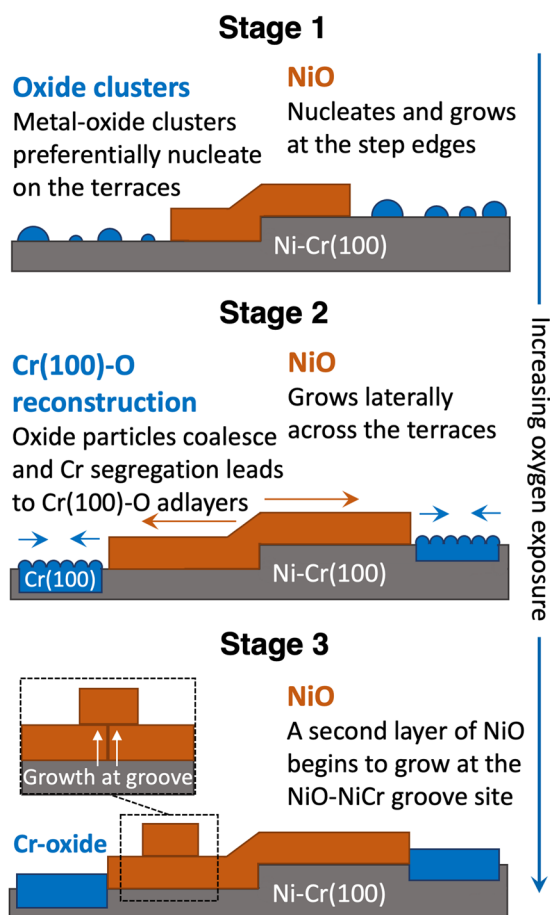


Fig. 7 A model for early-stage Ni–Cr(100) oxidation at 500 °C. Each stage of the oxidation process is highlighted with a diagram showing the evolution of each oxide product on the surface after low dosages of oxygen exposure, which increases from stage 1 to stage 3.

surface reflects the registry of the superlattice: averaged STS point spectra (~ 20 curves) comparing the groove sites (black dot) with the top sites (red dot) are shown in Fig. 6c and illustrate that the local variation in the local density of states (LDOS) is tied to differences in the valence band. The dI/dV curves indicate a 2×10^{-3} nA V⁻¹ relative decrease in the differential conductance at the groove site as compared to the top site. The corresponding band gap values from the entire LDOS map are summarized in Fig. 6d, and a visualization of the corresponding band gap map can be found in Supplementary Fig. 6, along with a valence band maximum map. The majority of the spectra yield a band gap of about 3.5 eV, however, the distribution is relatively broad. The electronic structure of the NiO across the superlattice is heterogeneous and signifies chemical differences imprinted by bonding at the NiO and Ni–Cr(100) interface. We propose that the preference for the initial nucleation of the next NiO layer at the groove sites is connected to local electronic structure variations and preferential diffusion paths for Ni created within the superlattice structure.

DISCUSSION

A general oxidation model is presented in Fig. 7, where the oxidation pathways of the Ni and Cr are partitioned and described over three stages. The oxidation of Ni–Cr(100) surfaces have revealed the nucleation and growth of NiO begin at the step edges, while Cr-rich oxide particles form on the terraces (stage 1). As oxygen exposure increases, NiO grows laterally, across the terraces, and a chromium-rich phase nucleates and grows on the surface, which is (partially) covered in Cr(100)–O adlayers triggered by local Cr-segregation (stage 2). Further oxidation causes the Ni–Cr(100) surface to become saturated with oxide and the NiO begins to grow vertically, primarily via the transport of Ni cations through the groove site in the superlattice, while the Cr-oxide grows into the alloy as subsurface Cr-oxide layers begin to form⁸.

The early-stage oxidation of Ni–Cr(100) alloy surfaces leads to structural and compositional changes along the alloy surface. After 7 L of O₂ exposure at 500 °C, changes in surface free energy initiate step-edge faceting via the growth of NiO wedges, low-

angle grain boundaries that mitigate strain at the oxide–alloy interface represented by the NiO–NiCr(7 × 8) superlattice, and the formation of oxide particles along the terraces and some of the step edges. At low partial pressures of O₂, these oxidation pathways will depend greatly on the adsorption of oxygen, which will be influenced by the d-bands of the Ni and Cr^{12,33,46–48}. Recently, it has been shown that Cr hybridizes more readily with the oxygen on Ni–Cr surfaces^{12,33}. These electronic effects enhance the propensity for oxygen adsorption at the Cr sites, supporting the assumption that the oxide particles on the Ni–Cr(100) surface are likely Cr-rich. Similar particles have also been observed on Cr(110) surfaces³², further bolstering this assignment, which indicates these clusters are a function of Cr concentration and local chemistry, not of crystallographic orientation. As such, the local clustering and bonding of Cr atoms at or near the surface are important for initiating the growth of a passive layer on Ni–Cr alloys. This behavior contrasts NiO growth, whose formation is favored by epitaxy.

The distribution of Cr across the first two planes of a Ni–Cr(100) surface was evaluated using a MATLAB code, where Cr cluster sizes >5 atoms increased significantly at about 15 at%Cr (~13 wt %). Given the size and shape of the oxide particles measured with our STM after 7 L, we can assume that the oxide particles are likely initiated on the filamentous Cr clusters, i.e., “strings” of Cr clusters. As a reaction to the initial O-adsorption event, the local Cr diffusion is favored through a chemical potential gradient and leads to the formation of clusters. While their formation is driven by the presence of Cr, they certainly can contain some Ni as a minor component.

After additional oxidation (14 L cumulative), as well as at stage 3 of the oxidation model, the NiO extends across the terraces and presents as a NiO–NiCr(6 × 7) superlattice. At these stages, the oxide particles are no longer visible. The oxide clusters are thermally stable⁷ but transform into the (chemisorption) oxygen adlayers during continued exposure, lowering the surface free energy and wetting the alloy surface. A variety of new surface structures with variable electronic signatures are now present. These have been observed on Ni–Cr(100) surfaces with smaller Cr content, but are only marginally related to surface structures on the corresponding pure metal surfaces. These chemisorbed adlayers are interpreted as metastable oxide phases, but their structures could not yet be resolved despite atomic resolution imaging (Supplementary Fig. 2). The large number of coexisting surface phases, which often only manifest at specific oxygen coverage and exposures, makes a conclusive structure resolution a daunting task.

With continued oxidation (18 L cumulative) the next layer of NiO has started to form, always propagating from the superlattice groove of the layer below. The electronic signature of the NiO superlattice, and specifically the valence band edge, is modulated following the geometry of the superlattice is a consequence of the registry at the NiO–NiCr interface. The next layer of the superlattice is always offset by half a superlattice cell and the grooves emerge as preferential nucleation sites. Distinct Cr(100)-p(2 × 2)O regions are also detected at this exposure and are identified by their geometric spacing and mostly metallic electronic signature. Adjacent to the p(2 × 2) regions, Cr-oxide rows and faceted Cr-oxide regions are observed. The Cr(100)-p(2 × 2)O reconstruction is found to form prior to the growth of a passive Cr-oxide layer and confirms the presence of BCC Cr(100) phase-separated regions. These regions are embedded in the alloy surface and serve as nucleation centers for Cr-oxide growth. Always adjacent to these segregated regions are Cr-oxide rows interpreted as an intermediate stage of chromia growth preceding the formation of a closed Cr-oxide layer. The faceted oxide regions, also attributed to the Cr oxidation pathway, are similarly found near phase-separated Cr(100) regions and are assigned to the advanced stages of Cr-oxide growth. The reaction pathway

towards the passive chromia layer is then described as a progression from BCC Cr(100) → Cr(100)-p(2 × 2)O → Cr-oxide rows → faceted Cr-oxide. These results support the formation of phase-separated BCC Cr(100) layers on the surface which predicate the formation of a passive chromia layer on Ni–Cr(100).

The oxide growth kinetics can be described with well-known kinetic functions, which are applicable once a full oxide layer has formed. Once this stage has been reached the relevant reactions for oxide thickening such as cation diffusion, vacancy motion, or O-diffusion from the surface to the oxide–metal interface control the oxidation kinetics. In the very early stages of oxidation covered in our work, different parts of the sample will express different kinetics—for example, initially, the motion of the NiO growth front is likely dominated by the capture of oxygen atoms, which transfer from the chemisorbed to the ionically bonded state, whereas the transition from Cr–O reconstructions to Cr-oxide is governed by a different set of reactions. Therefore, which reactions control the overall kinetics and rates will depend on the individual oxide species and their reactive pathway. These will need to be considered in more detail, and piecewise kinetic functions developed, to understand how passivation initiates at these early stages of oxidation.

The oxidation pathways of Ni–Cr alloys have been investigated by studying the evolution of partial surface oxides on a Ni–15 wt% Cr(100) sample. In this compositional space, the crystal structure of the alloy consists of a random solid solution of Cr atoms within an FCC Ni(100) lattice, however, the progression of the Ni and Cr oxidation pathways drive changes to the crystal structure and chemistry of the Ni–Cr alloy surface. Step-edge faceting was observed where NiO growth initiated, while step edges with Cr-rich oxide particles remained curved. As oxidation progressed the surface phase separation of BCC Cr(100) is confirmed via the observation of a Cr(100)-p(2 × 2)O reconstruction. Neighboring these regions several areas with what is currently interpreted as Cr-oxide rows, and faceted Cr-oxide features were found, each displaying a unique electronic signature. As the alloy surface became increasingly saturated, next layer NiO growth initiated at the groove of the superlattice, which displayed electronic heterogeneity imprinted by the alloy–oxide interface. Understanding the oxidation pathways of partial oxide layers on Ni–Cr(100) alloys has given insight into the manner in which binary alloy systems undergo passivation within the pre-Cabrera–Mott regime.

METHODS

Experimental

Each step of the oxidation experiment was conducted in situ under UHV conditions using an Omicron Nanotechnology Variable Temperature Scanning Probe Microscopy (VT-SPM) system. The base pressure during measurements was kept at 3.0×10^{-10} mbar and imaging was conducted with an electrochemically prepared tungsten tip at ambient temperature. Using electron beam evaporation, the Ni–15 wt%Cr(100) thin film was grown using Ni (Alfa Aesar 99.999% purity) and Cr (American Elements, 99.95% purity), which were deposited on pretreated MgO(100) single crystal substrates³⁰. Prior to the alloy thin film growth, the deposition rates of the Ni and Cr were measured using a quartz crystal monitor to accurately adjust the film composition. The deposition of the Ni–15 wt%Cr(100) thin-film followed the procedure reported previously³⁰. The starting alloy surface was found to have wide round terraces and the cleanliness and metallicity of the surface are confirmed by STS, Supplementary Fig. 7. Oxygen was introduced through a sapphire leak valve while the Ni–Cr(100) sample was held at a constant elevated temperature of 500 °C and once the sample had cooled, the alloy surface was imaged at each oxidation step. Oxidation steps of +7 L ($p[\text{O}_2] = 7 \times 10^{-9}$ mbar, $t = 1330$ s), +7 L ($p[\text{O}_2] = 7 \times 10^{-9}$ mbar, $t = 1330$ s), and +4 L ($p[\text{O}_2] = 4 \times 10^{-9}$ mbar, $t = 1330$ s), for a cumulative of 18 L of O₂ exposure, were used to achieve partial oxide growth on the surface. One L (Langmuir) corresponds to 1 s exposure at 1.33×10^{-6} mbar of $p[\text{O}_2]$ and is equivalent to a monolayer of adsorbed molecules assuming a sticking coefficient of one. The composition of the alloy film was verified ex situ by energy dispersive spectroscopy

with a Quanta LV650 scanning electron microscope where the composition at five different spots on the film surface was averaged and a standard deviation of 0.38 wt% calculated from these results.

The surface topography and LDOS of the sample were measured before and after oxidation by STM and STS. The grid spectra were captured by sweeping the bias voltage (V_{bias}) from ± 3.0 V and measuring an I/V curve for every fourth image pixel with an open current feedback loop. Simultaneously, the topography information was recorded for the next three pixels, where the tunneling current (I_t) was set at $I_t = 0.1$ nA and a bias voltage $V_{\text{bias}} = 3.0$ V was used. The I/V curves were numerically differentiated to generate dI/dV curves, which are then normalized by $(dI/dV)/(I/V)$ following the procedure described by Feenstra et al.^{49,50}. The band gap was numerically determined from the normalized curves, by calculating the region where $(dI/dV)/(I/V)$ is smaller than a threshold value, i.e., where the DOS is effectively zero, and distributions of valence/conduction band extrema and band gap values were generated from these data. The $(dI/dV)/(I/V)$ spectra are then spatially resolved by selecting a specific voltage slice (e.g., $V_{\text{slice}} = -2.7$ V) to highlight the contrast in local electronic structure at that particular voltage and displayed as a DOS map. This allows for the direct comparison between topography and electronic structure. Prior to the display and analysis of the topography images, each surface was leveled by mean plane subtraction and planarization using the post-processing software Gwyddion⁵¹. A MATLAB code implementing routines for gray-scale segmentation was also used to analyze some of the surface features and is highlighted in Supplementary Fig. 8.

Monte Carlo simulation

To better understand the clustering of Cr atoms within the Ni lattice, an in-house MATLAB code was written that modeled the first two surface planes of the lattice and identified clusters of adjacent Cr atoms. Matrices were used to represent atom planes of the (100) surface and a random number generator probabilistically assigned a 1 (Cr) or 0 (Ni) to each position in a square matrix corresponding to the atomic coordinates of an FCC Ni lattice (Supplementary Fig. 1). Two such planes were created representing the (i) top surface plane and (ii) the plane below the surface, properly offset to simulate an FCC (100) surface. Inter-atomic forces are not taken into account, so the occupation of each site is random, and the formation of clusters is therefore only a consequence only of probability. Clusters of Cr atoms were identified by finding Cr atoms and recursively checking all adjacent positions (eight positions in the same plane and four in the other plane) for other Cr atoms until no more are found. These clusters were then categorized by size (i.e., the number of Cr atoms in the cluster) and visualized via subroutines in the code. No distinction was made between Cr atoms that were adjacent laterally, diagonally, or from different planes, and a periodic boundary condition was used to eliminate edge effects. Only the Cr atoms in the top two (100) planes were considered, but the program mandated that at least one Cr atom in each cluster must be on the top surface plane to be counted since this is interpreted as the primary reaction site (Supplementary Fig. 1).

DATA AVAILABILITY

Both the experimental and computational data from this report will be made available upon a reasonable request from the corresponding author.

CODE AVAILABILITY

The codes used to determine the LDOS and band gap maps, as well as the Monte-Carlo code used for the Cr clustering statistics, can be provided upon a reasonable request from the authors.

Received: 27 January 2021; Accepted: 15 March 2021;

Published online: 12 April 2021

REFERENCES

- Atkinson, A. Transport processes during the growth of oxide films at elevated temperature. *Rev. Mod. Phys.* **57**, 437–470 (1985).
- Wood, G. C. & Chattopadhyay, B. Transient oxidation of Ni-base alloys. *Corros. Sci.* **10**, 471–480 (1970).
- Chattopadhyay, B. & Wood, G. C. The transient oxidation of alloys. *Oxid. Metals* **2**, 373–399 (1970).
- Mohanty, P., Rath, C., Mallick, P., Biswal, R. & Mishra, N. C. UV-visible studies of nickel oxide thin film grown by thermal oxidation of nickel. *Phys. B Condens. Matter* **405**, 2711–2714 (2010).
- Haugrud, R. On the high-temperature oxidation of nickel. *Corros. Sci.* **45**, 211–235 (2003).
- Ma, L., Wiame, F., Maurice, V. & Marcus, P. Origin of nanoscale heterogeneity in the surface oxide film protecting stainless steel against corrosion. *Npj Mater. Degrad.* **3**, 1–9 (2019).
- Blades, W. H. & Reinke, P. From alloy to oxide: capturing the early stages of oxidation on Ni–Cr(100) alloys. *ACS Appl. Mater. Interfaces* **10**, 43219–43229 (2018).
- Luo, L. et al. In-situ transmission electron microscopy study of surface oxidation for Ni–10Cr and Ni–20Cr alloys. *Scr. Mater.* **114**, 129–132 (2016).
- Luo, L. et al. In situ atomic scale visualization of surface kinetics driven dynamics of oxide growth on a Ni–Cr surface. *Chem. Commun.* **52**, 3300–3303 (2016).
- Ramanathan, R., Ramalingam, G., Perepezko, J. H., Reinke, P. & Voorhees, P. W. Evolution of NiO island size distributions during the oxidation of a Ni–5Cr alloy: experiment and modeling. *ACS Appl. Mater. Interfaces* (2018) <https://doi.org/10.1021/acsami.7b18539>.
- Gusieva, K. et al. Repassivation behavior of individual grain facets on dilute Ni–Cr and Ni–Cr–Mo alloys in acidified chloride solution. *J. Phys. Chem. C* **122**, 19499–19513 (2018).
- Sprowl, L. H., Adam, B. M., Tucker, J. D. & Árnadóttir, L. First-principles study of the products of CO₂ dissociation on nickel-based alloys: trends in energetics with alloying element. *Surf. Sci.* **677**, 219–231 (2018).
- Lutton, K., Gusieva, K., Ott, N., Birbilis, N. & Scully, J. R. Understanding multi-element alloy passivation in acidic solutions using operando methods. *Electrochem. Commun.* **80**, 44–47 (2017).
- Yu, X. et al. Nonequilibrium solute capture in passivating oxide films. *Phys. Rev. Lett.* **121**, 145701 (2018).
- Lutton, K., Blades, W. H., Scully, J. R. & Reinke, P. Influence of chloride on nanoscale electrochemical passivation processes. *J. Phys. Chem. C* **124**, 9289–9304 (2020).
- Cabrera, N. & Mott, N. F. Theory of the oxidation of metals. *Rep. Prog. Phys.* **12**, 163 (1949).
- Seyoux, A., Maurice, V. & Marcus, P. Oxide film growth kinetics on metals and alloys I. Physical model. *J. Electrochem. Soc.* **160**, C189–C196 (2013).
- Kopatzki, E. & Behm, R. J. Step faceting: origin of the temperature dependent induction period in Ni(100) oxidation. *Phys. Rev. Lett.* **74**, 1399–1402 (1995).
- Bäumer, M. et al. The structure of thin NiO(100) films grown on Ni(100) as determined by low-energy-electron diffraction and scanning tunneling microscopy. *Surf. Sci.* **253**, 116–128 (1991).
- Smeenk, R. G., Tromp, R. M., Frenken, J. W. M. & Saris, F. W. The oxidation of Ni (100) studied by medium energy ion scattering. *Surf. Sci.* **112**, 261–271 (1981).
- Kopatzki, E. & Behm, R. J. STM imaging and local order of oxygen adlayers on Ni (100). *Surf. Sci.* **245**, 255–262 (1991).
- Stuckless, J. T. et al. Oxygen chemisorption and oxide film growth on Ni(100), {110}, and {111}: Sticking probabilities and microcalorimetric adsorption heats. *J. Chem. Phys.* **106**, 2012–2030 (1997).
- Foord, J. S. & Lambert, R. M. Oxygen chemisorption and corrosion on Cr(100) and Cr(110) single crystal surfaces. *Surf. Sci.* **161**, 513–520 (1985).
- Hope, G. A. & Ritchie, I. M. The oxidation of thin chromium films. *Thin Solid Films* **34**, 111–114 (1976).
- Salomonsen, G., Norman, N., Lonsjo, O. & Finstad, T. G. Kinetics and mechanism of oxide formation on Cr thin films. *J. Phys. Condens. Matter* **1**, 7843 (1989).
- Peter, R., Saric, I., Piltaver, I. K., Badovinac, I. J. & Petracic, M. Oxide formation on chromium metal surfaces by low-energy oxygen implantation at room temperature. *Thin Solid Films* **636**, 225–231 (2017).
- Schmid, M. et al. Oxygen-induced vacancy formation on a metal surface. *Phys. Rev. Lett.* **82**, 355–358 (1999).
- Arlow, J. S., Mitchell, D. F. & Graham, M. J. The mechanism and kinetics of the oxidation of Cr(100) single-crystal surfaces studied by reflection high-energy electron diffraction, x-ray emission spectroscopy, and secondary ion mass spectrometry/Auger sputter depth profiling. *J. Vac. Sci. Technol. A* **5**, 572–576 (1987).
- Chien, S.-C. & Windl, W. Bond synergy model for bond energies in alloy oxides. *J. Electrochem. Soc.* **167**, 141511 (2020).
- Ramalingam, G. & Reinke, P. Growth of Ni and Ni–Cr alloy thin films on MgO(001): effect of alloy composition on surface morphology. *J. Appl. Phys.* **120**, 225302 (2016).
- Saiki, R. S., Kaduwela, A. P., Osterwalder, J., Fadley, C. S. & Brundle, C. R. Observation and characterization of a strained lateral superlattice in the oxidation of Ni (001). *Phys. Rev. B* **40**, 1586–1592 (1989).
- Maurice, V., Cadot, S. & Marcus, P. XPS, LEED and STM study of thin oxide films formed on Cr(110). *Surf. Sci.* **458**, 195–215 (2000).
- Samin, A. J. & Taylor, C. D. First-principles investigation of surface properties and adsorption of oxygen on Ni–22Cr and the role of molybdenum. *Corros. Sci.* **134**, 103–111 (2018).
- Maurice, V., Despert, G., Zanna, S., Bacos, M.-P. & Marcus, P. Self-assembling of atomic vacancies at an oxide/intermetallic alloy interface. *Nat. Mater.* **3**, 687–691 (2004).

35. Wyckoff, R. W. G. Crystal structures. vol. 1 (Interscience Publishers, 1963).
36. Howe, J. M. 14—Structure, composition and energy of solid–solid interfaces. In *Physical Metallurgy* (Fifth Edition) (eds Laughlin, D. E. & Hono, K.) 1317–1451 (Elsevier, 2014). <https://doi.org/10.1016/B978-0-444-53770-6.00014-9>.
37. Chen, J. K., Farkas, D. & Reynolds, W. T. Atomistic simulation of an f.c.c./b.c.c. interface in Ni–Cr alloys. *Acta Mater.* **45**, 4415–4421 (1997).
38. Rigsbee, J. M. & Aaronson, H. I. A computer modeling study of partially coherent f.c.c./b.c.c. boundaries. *Acta Metals* **27**, 351–363 (1979).
39. Hall, M. G., Aaronson, H. I. & Kinsma, K. R. The structure of nearly coherent fcc: bcc boundaries in a Cu–Cr alloy. *Surf. Sci.* **31**, 257–274 (1972).
40. Bikondoa, O. et al. Impact of ambient oxygen on the surface structure of alpha-Cr₂O₃(0001). *Phys. Rev. B* **81**, 205439 (2010).
41. Cao, S. et al. The surface stability of Cr₂O₃(0001). *J. Phys. Condens. Matter* **27**, 255003 (2015).
42. Lübke, M. & Moritz, W. A LEED analysis of the clean surfaces of alpha-Fe₂O₃(0001) and alpha-Cr₂O₃(0001) bulk single crystals. *J. Phys. Condens. Matter* **21**, 134010 (2009).
43. Rohr, F. et al. Strong relaxations at the Cr₂O₃(0001) surface as determined via low-energy electron diffraction and molecular dynamics simulations. *Surf. Sci.* **372**, L291–L297 (1997).
44. Rohrbach, A., Hafner, J. & Kresse, G. Ab initio study of the (0001) surfaces of hematite and chromia: influence of strong electronic correlations. *Phys. Rev. B* **70**, 125426 (2004).
45. Chattopadhyay, B. & Wood, G. C. The transient oxidation of Fe–Cr and Ni–Cr alloys. *J. Electrochem. Soc.* **117**, 1163 (1970).
46. Hammer, B. & Nørskov, J. K. Why gold is the noblest of all the metals. *Nature* **376**, 238–240 (1995).
47. Hammer, B. & Nørskov, J. K. Electronic factors determining the reactivity of metal surfaces. *Surf. Sci.* **343**, 211–220 (1995).
48. Hammer, B. & Nørskov, J. K. Theoretical surface science and catalysis—calculations and concepts. In *Advances in Catalysis* vol. 45 71–129 (Academic Press, 2000).
49. Feenstra, R. M. Tunneling spectroscopy of the (110) surface of direct-gap III–V semiconductors. *Phys. Rev. B* **50**, 4561–4570 (1994).
50. Feenstra, R. M., Stroscio, J. A. & Fein, A. P. Tunneling spectroscopy of the Si(111) 2 × 1 surface. *Surf. Sci.* **181**, 295–306 (1987).
51. Nečas, D. & Klapetek, P. Gwyddion: an open-source software for SPM data analysis. *Open Phys.* **10**, 181–188 (2011).

ACKNOWLEDGEMENTS

W.H.B. and P.R. would like to thank the Office of Naval Research for supporting the MURI Program entitled “Corrosion in 4D,” Grant N00014-14-1-0675, under program manager Dr. David Shifler.

AUTHOR CONTRIBUTIONS

W.H.B. performed the experiment, wrote the manuscript and analyzed the data. M.R. B. wrote the MATLAB code that was used to quantify the Cr distribution and provided analysis of the data. P.R. conceived and guided the study, and co-wrote the manuscript. All authors contributed to the interpretation of the work, edited the manuscript and approved the final version.

COMPETING INTERESTS

The authors declare no competing interests.

ADDITIONAL INFORMATION

Supplementary information The online version contains supplementary material available at <https://doi.org/10.1038/s41529-021-00164-7>.

Correspondence and requests for materials should be addressed to P.R.

Reprints and permission information is available at <http://www.nature.com/reprints>

Publisher’s note Springer Nature remains neutral with regard to jurisdictional claims in published maps and institutional affiliations.



Open Access This article is licensed under a Creative Commons Attribution 4.0 International License, which permits use, sharing, adaptation, distribution and reproduction in any medium or format, as long as you give appropriate credit to the original author(s) and the source, provide a link to the Creative Commons license, and indicate if changes were made. The images or other third party material in this article are included in the article’s Creative Commons license, unless indicated otherwise in a credit line to the material. If material is not included in the article’s Creative Commons license and your intended use is not permitted by statutory regulation or exceeds the permitted use, you will need to obtain permission directly from the copyright holder. To view a copy of this license, visit <http://creativecommons.org/licenses/by/4.0/>.

© The Author(s) 2021